Optical Materials 57 (2016) 169–173

Contents lists available at ScienceDirect

Optical Materials

journal homepage: www.elsevier.com/locate/optmat

Femtosecond laser written optical waveguides in *z*-cut MgO:$LiNbO_3$ crystal: Fabrication and optical damage investigation

Jinman Lv [a], Yazhou Cheng [a], Qingming Lu [b], Javier R. Vázquez de Aldana [c], Xiaotao Hao [a, **], Feng Chen [a, *]

[a] School of Physics, State Key Laboratory of Crystal Materials, Shandong University, Jinan 250100, China
[b] School of Chemistry and Chemical Engineering, Shandong University, Jinan 250100, China
[c] Laser Microprocessing Group, Universidad de Salamanca, Salamanca 37008, Spain

ARTICLE INFO

Article history:
Received 12 April 2016
Received in revised form
30 April 2016
Accepted 2 May 2016
Available online 8 May 2016

Keywords:
Optical waveguide
MgO:$LiNbO_3$ crystal
Femtosecond laser inscription
Optical damage

ABSTRACT

We report on the fabrication of the dual-line waveguides and cladding waveguide in *z*-cut MgO:$LiNbO_3$ crystal by femtosecond laser inscription. Due to the diverse modification of refractive index along TE/TM polarization induced by femtosecond laser pulses, the two geometries exhibit different guiding performances: the dual-line waveguides only support extraordinary index polarization, whilst the depressed cladding waveguide supports guidance along both extraordinary and ordinary index polarizations. The measured optical damage of these waveguides at the wavelength of 532 nm is higher than that of the previously reported ion-implanted waveguides in Zr-doped $LiNbO_3$. The propagation loss of depressed cladding waveguide is measured as low as 0.94 dB/cm at 632.8 nm wavelength. It is found that the optical damage threshold (~10^5 W/cm^2) of the dual-line waveguide is one order of magnitude higher than that of the cladding waveguide (~10^4 W/cm^2).

1. Introduction

As one of the most well-known multifunctional crystals, lithium niobate ($LiNbO_3$ or LN) has been widely applied in a variety of photonic devices including switches, modulators, multiplexers and waveguide amplifiers, owing to its unique electro-optic, acousto-optic, piezoelectric, and nonlinear properties [1–5]. In integrated photonics and modern optical communication systems, optical waveguides are fundamental elements that could confine light propagating within extremely small volumes with size of several micrometers, in which the optical intensities can reach a much higher level with respect to the bulk. Benefiting from the small size of the configurations, it is easy to combine compact optical circuits or chips with other photonic components for quite various applications [6]. Although the conventional pure LN crystals possess large nonlinear optical properties, the relatively low optical damage threshold prevents its application in high-power circumstances [7]. It has been demonstrated that doping of 4.6 or more atomic percent of Mg^{2+} into LN has the ability to improve the optical damage resistance about one hundred times as great as pure LN [8].

Several techniques have been applied to fabricate diverse waveguides in various materials, such as metal-ion indiffusion [9], ion implantation/irradiation [10–12], and ultrafast laser writing [13–17]. The microprocessing with ultrafast lasers with tens or hundreds of femtoseconds (fs) pulses has recently become one of the most powerful and efficient methods to construct direct waveguides in various transparent optical materials, including amorphous glasses, single crystals, polycrystalline ceramics, organic polymers, etc. [18–21]. The refractive index modification of the targets by fs-laser inscription is impacted by both the laser parameters (pulse duration, repetition rate, and pulse energy, scanning speed, focusing condition) and material properties [22–25]. According to the relative position from the fs-laser-induced tracks, the fs-laser written waveguides can be classified into three types: Type I (directly written waveguides, which located inside the fs-laser-induced tracks with positive refractive-index changes), Type II (stress-induced waveguides or dual-line waveguides locating in the adjacent regions of the fs-laser-induced tracks with negative refractive-index changes), and depressed cladding waveguides consisting of a core surrounded by a number of low-index tracks (sometimes called Type III guiding geometry)

* Corresponding author.
** Corresponding author.
E-mail addresses: haoxt@sdu.edu.cn (X. Hao), drfchen@sdu.edu.cn (F. Chen).

http://dx.doi.org/10.1016/j.optmat.2016.05.003
0925-3467/

[26]. In crystals, compared with geometry of Type I modification, the dual-line and depressed cladding waveguide configurations have two advantages. One is that the bulk features in the waveguides may not be affected conspicuously owing to the waveguides core locating in the region between the damaged tracks; the other is that the dual-line waveguide and depressed cladding waveguide structures can more easily control the refractive-index change of the tracks. As of yet, structures of Type I to III have all been realized in $LiNbO_3$ crystals by fs-laser writing technique [27–29].

In this work, we fabricated dual-line waveguides and depressed cladding waveguide by femtosecond-laser inscription in the z-cut MgO:$LiNbO_3$ crystal. The optical guiding properties along different polarizations, optical damage properties and micro-Raman spectra of the dual-line waveguides and depressed cladding waveguide in MgO:$LiNbO_3$ crystal were investigated in detail.

2. Experiments in details

The optically polished *z*-cut MgO:$LiNbO_3$ crystals (doped by 6.5 at. % Mg^{2+} ions) used in this work was cut into wafers with a size of 7.24 (x) × 9 (y) × 1 (z) mm^3. Three dual-line waveguides (labeled by WG1, WG2, and WG3, respectively) and one depressed cladding (labeled by WG4) with circular cross section were fabricated by utilizing the laser facilities at the Universídad de Salamanca. An amplified Ti:Sapphire laser system (Spitfire, Spectra Physics, USA) was employed as a laser source which generated linearly polarized pulses of 120 fs, 1 mJ maximum pulse energy at a repetition rate of 1 kHz and the central wavelength of 795 nm. The pulse energy used to irradiate waveguide was controlled by a calibrated neutral density filter, a half-wave plate and a linear polarizer. During the irradiation, the sample was placed at a micro-positioning 3-axes motorized stages with the setting velocity and direction controlled by the computer. One 20 × microscope objective (N.A. = 0.40) was applied to focus the laser at the depth of 75 μm under the largest sample surface (dimensions of 7.24 × 9 mm^2). Several tests at different pulse energies and scanning velocities were performed, and we looked through an optical microscopy (in transmission mode) to assess the damage tracks produced in the sample. Finally, the pulse energy was fixed to 2.1 μJ for all waveguides, and the scanning velocity was set to 20 μm/s, 50 μm/s, 100 μm/s, 500 μm/s along *x*-axis for WG1-WG4, respectively. Afterward, to improve the waveguides qualities, we employed thermal annealing treatment at 260 °C for 1 h in open air.

The microscope images of the waveguides cross sections were observed by a polarized microscope (Axio Imager, Carl Zeiss). To investigate the near-field modal profiles of the waveguides, we used an end-face coupling arrangement with a linearly polarized He–Ne laser at a wavelength of 632.8 nm. A pair of microscope objective lenses (N.A. = 0.4) were utilized to couple the light beam into and out of the waveguides. Afterwards, a CCD which was connected to a computer recorded the modal profiles along both TE and TM polarizations. To calculate the propagation losses of the waveguides, we measured the input and output light beam power of the waveguides by using a powermeter, and estimated the coupling efficiency (e.g., the overlap of waveguide modes and incident light beam profiles) and the Fresnel reflection of waveguides. We also measured the N.A. of the waveguide to get the maximum value of refractive index changes of the waveguide by adjusting the position of the incident coupled light.

Based on the end-face coupling system, we estimated the optical damage resistance of MgO:$LiNbO_3$ waveguides by using a Coherent Verdi-8 laser source to generate 532 nm light as probe beams. Additionally, an optical attenuator was employed to control the intensity of incident laser beam. Afterward, we employed a powermeter to measure the input and output light power every 5 minutes.

In order to study the physical mechanism of femtosecond laser written MgO:$LiNbO_3$ waveguide formation, a confocal micro-Raman spectra-meter was used to measure the Raman properties. A continuous-wave laser beam at wavelength of 531.89 nm was focused onto the end facet of dual-line waveguide (WG1), depressed cladding waveguide (WG4) and bulk regions, respectively.

3. Results and discussion

Fig. 1(a)–(d) show the optical microscope images of the cross sections of the MgO: $LiNbO_3$ dual-line waveguides and depressed cladding waveguide, respectively. As we can see from Fig. 1(a)–(c), three dual-line waveguides WG1-WG3 have two tracks with separation of 15 μm. The core of the dual-line waveguides is located between these two filaments. As depicted in Fig. 1(d), the depressed cladding waveguide core is located in the circular geometry region and surrounded by a number of parallel femtosecond laser inscribed tracks with a lateral separation of ~3 μm between adjacent scans. The diameter of the depressed cladding waveguide (WG4) is ~30 μm.

As the MgO:$LiNbO_3$ sample is *z*-cut, the TM modal distributions correspond to the extraordinary index (n_e) polarization, while the TE modal distributions correspond to the polarization along ordinary index (n_o). As one can see, for the dual-line waveguides WG1-WG3 the near-field modal distributions exhibit fundamental modes for n_e polarization at 632.8 nm, which are shown in Fig. 2(a)–(c). However, whether before or after the annealing treatment, we can not achieve the near-field modal profile along n_o polarization, which is in agreement with the theoretical estimation from the guided-wave optics [30]. Fig. 2(d) and (e) depict the measured near-field modal profiles of the TM and TE modes of depressed cladding waveguide WG4. As one can see, WG4 shows multimode along the two polarizations. However, WG4 shows better symmetric quasi-circular distribution along TE polarization than that of TM polarization.

By assuming a step-like refractive index profile and measuring the numerical aperture of the waveguides, we estimate the refractive index contrasts of MgO:$LiNbO_3$ dual-line waveguides and depressed cladding waveguide. We measure the maximum incident angle Θ_m at which no change of the transmitted power is occurring. Finally, we can approximately calculate the maximum refractive index change in the waveguide using the formula [31].

$$\Delta n = \frac{\sin^2 \Theta_m}{2n} \tag{1}$$

where $n_e = 2.2022$ and $n_o = 2.2864$ are the refractive index of the bulk at 632.8 nm wavelength. In our work, the calculated maximum refractive index alternations (Δn_e) are ~3.96×10^{-3}, ~3.24×10^{-3}, and ~2.31×10^{-3} for the TM modes of MgO:$LiNbO_3$ dual-line waveguides WG1-WG3, respectively. It could be clearly seen that the three dual-line waveguides fabricated with the same energy and diameter but different scanning velocities ($v_1 < v_2 < v_3$) exhibit different refractive index alternations ($\Delta n_1 > \Delta n_2 > \Delta n_3$). It is to say that the refractive index alternations increase by reducing the scanning velocity. For the depressed cladding waveguide WG4, the value of refractive index alternations for n_e polarization is 1.45×10^{-3}, which is smaller than that for n_o polarization 3.13×10^{-3}. Experimentally, the larger value of refractive index alternations may lead to the superior guiding properties along n_o polarization, which could obviously be seen from Fig. 2(d) comparing to Fig. 2(e).

Based on the obtained Δn, the 2D refractive index profiles of the

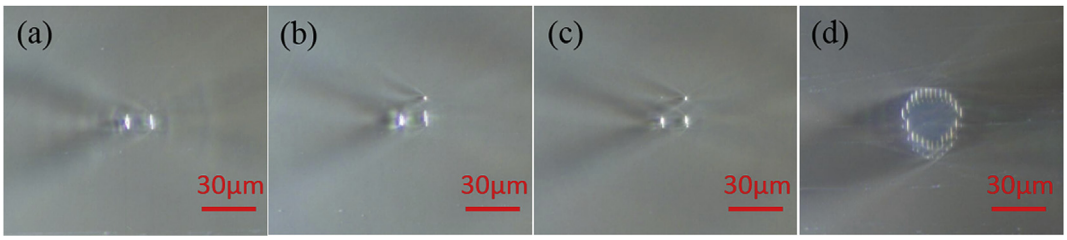

Fig. 1. Optical microscope images of the cross sections of the dual-line waveguides (a) WG1 (b) WG2 (c) WG3 and (d) the depressed cladding waveguide WG4.

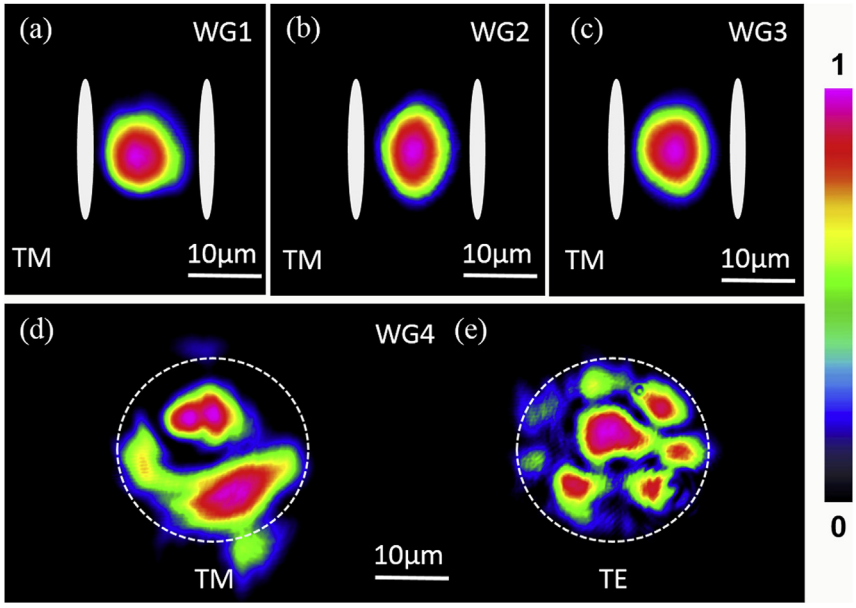

Fig. 2. Measured near-field intensity distributions for the TM modes of the dual-line waveguides (a) WG1 (b) WG2 (c) WG3, and that of the cladding waveguide at (d) TM mode and TE mode. The dashed lines and circles indicate the spatial locations of the boundaries of the waveguide structures.

dual-line waveguides could be reconstructed with the same technique introduced in previous work [32]. We reconstructed 2D refractive index profile at the cross section of MgO:$LiNbO_3$ dual-line waveguide WG1 along the n_e polarization, as shown in Fig. 3(a). Afterwards, we simulated the light propagation at 632.8 nm by using BeamPROP (Rsoft®) software, which is based on the reconstructed 2D refractive index profile and the theory of the finite-difference beam propagation method (FD-BPM) [33,34]. Fig. 3(b) shows the calculated modal profile of WG1 along the TM polarization in MgO:$LiNbO_3$ crystal. By comparing Fig. 3(b) with Fig. 2(a), one can see that the calculated profile is in agreement with the experimental result. Therefore, it is proved that the reconstructed

Table 1
Propagation losses α of MgO:$LiNbO_3$ waveguides WG1–WG4 for n_e and n_o polarizations at 632.8 nm after annealing treatments.

Waveguides	Propagation loss (dB/cm)	
	TM (n_e)	TE (n_o)
WG1	2.73	–
WG2	3.28	–
WG3	4.42	–
WG4	2.57	0.94

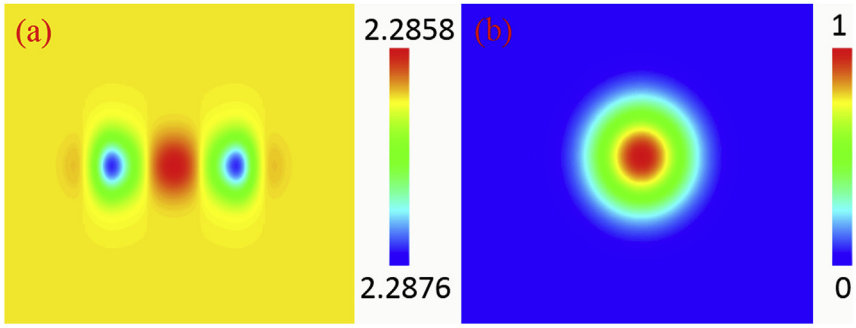

Fig. 3. (a) Reconstructed 2D refractive index profile at the cross section and (b) calculated modal profile of dual-line MgO:$LiNbO_3$ waveguide WG1 of TM polarization at 632.8 nm.

refractive index profile of the dual-line waveguide is reasonable.

Table 1 shows the propagation losses (α) of the dual-line waveguides WG1-WG3 on TM polarization and depressed cladding waveguide WG4 along both TM and TE polarizations at 632.8 nm. For dual-line waveguides, the coupling loss is estimated to be ~1.7 dB for all waveguides and the propagation losses show $\alpha_3 > \alpha_2 > \alpha_1$ along n_e polarization. For depressed cladding waveguide WG4, the coupling loss is estimated to be ~1.2 dB for both TM and TE polarizations and the propagation loss along n_e polarization is larger than the values measured along n_o polarization. It indicates that as the refractive index alternation of the waveguide increases, the propagation loss becomes lower. Through the comparison, one can see that the propagation loss of depressed cladding waveguide is smaller than those of the all dual-line waveguides, which is in good agreement of the previous work [35]. Fig. 4 shows the all-angle output light power to investigate the thorough information of the polarization effects of the guidance with the input light power of 1.585 mW. As one can see, for all the dual-line waveguides and depressed cladding waveguide, the output light intensity will change accordingly with the change of the light polarization angle, which shows the sensitivity of polarization guidance. Fig. 4(a) depicts the output power of the dual-line waveguides showing $P_1 > P_2 > P_3$. Particularly, comparing Fig. 4(a) with Fig. 4(b), there is distinct characteristics of polarization sensitive between dual-line waveguides and depressed cladding waveguide. For the dual-line waveguides, the output power approaches zero when the polarization angles are 0° and 180°, while the output power reaches maximum with 90° and 270° of the TM polarization, as shown in Fig. 4(a). It means that the refractive index change along TE polarization is so small that it cannot confine the light propagation efficiently, while the refractive index change along TM polarization is large enough to guide the light propagation. However, for the depressed cladding waveguide, Fig. 4(b) depicts the polarization direction of the maximum and the minimum of the output power is contrary to the dual-line waveguides. These results are in agreement with the theoretical estimations from the guided-wave optics [30].

Fig. 5(a) and (b) depict the measured output intensity as the function of the input intensity at 532 nm from the MgO:$LiNbO_3$ dual-line waveguides WG1-WG3 and cladding waveguide WG4, respectively. The diverse dots and lines are the experimental data and linear fits, respectively. As shown in the two figures, one can see that as the input intensity increase, the output intensity is no longer proportional to the input intensity, which means that they reach the optical damage thresholds of these waveguides. From the linear fit of the experimental data, we have determined that the optical damage thresholds are ~1.03 × 10^5, ~1.14 × 10^5, and ~1.38 × 10^5 W/cm^2 for the dual-line waveguides WG1-WG3, respectively, and that is ~2.40 × 10^4 for the depressed cladding waveguide WG4. In previous works for $LiNbO_3$, the optical damage thresholds of the 4 mol% Zr^{4+}-doped $LiNbO_3$ planar waveguides and 5 μm-width ridge waveguide produced by proton implantation are 2.8 × 10^3 W/cm^2 and 9.2 × 10^4 W/cm^2, respectively [36]. As of yet, the measured the optical damage threshold of the MgO:$LiNbO_3$ (doped by 6.5 at.% Mg^{2+} ions) 15 μm-width ridge waveguide fabricated by swift O^{5+} ion irradiation is 5.6 × 10^3 W/cm^2. The results for the waveguides inscribed by femtosecond laser exhibit higher optical damage resistance than those of the ion implanted pure $LiNbO_3$ waveguides.

Fig. 6 shows the micro-Raman spectra of the MgO:$LiNbO_3$ crystal at the regions of the dual-line waveguide (WG1), cladding waveguide (WG4) and the bulk at room-temperature. In the range of Raman shift from 100 to 800 cm^{-1}, the sharp peaks at 153, 239, 264, 325, 370, 436, 580 and 634 cm^{-1} are detected and labeled. As one can see, the spectra of WG1 and WG4 have similar peak widths and peak positions with respect to those in the bulk region, while the peak intensities of WG1 and WG4 averagely increase about 30% and 8% with respect to the bulk, respectively. It indicates that there is lattice modification to some extent induced by femtosecond laser inscription, which is below the lattice changing threshold of MgO:$LiNbO_3$ crystal.

4. Conclusion

We report on the fabrication of dual-line waveguides and cladding waveguide in MgO:$LiNbO_3$ crystal by femtosecond laser inscription. The dual-line waveguides support only extraordinary index polarization, while the depressed cladding waveguide supports guidance both along extraordinary and ordinary index polarizations. The experimentally measured modal profile of the dual-line waveguide is in good agreement with the result based on the simulation. The optical damage threshold of the dual-line waveguide is larger than that of the cladding waveguide, and as the scanning velocity increases, the optical damage threshold becomes larger. In addition, compared with ion-implanted waveguides in Zr:$LiNbO_3$ and MgO:$LiNbO_3$, the MgO:$LiNbO_3$ waveguides by

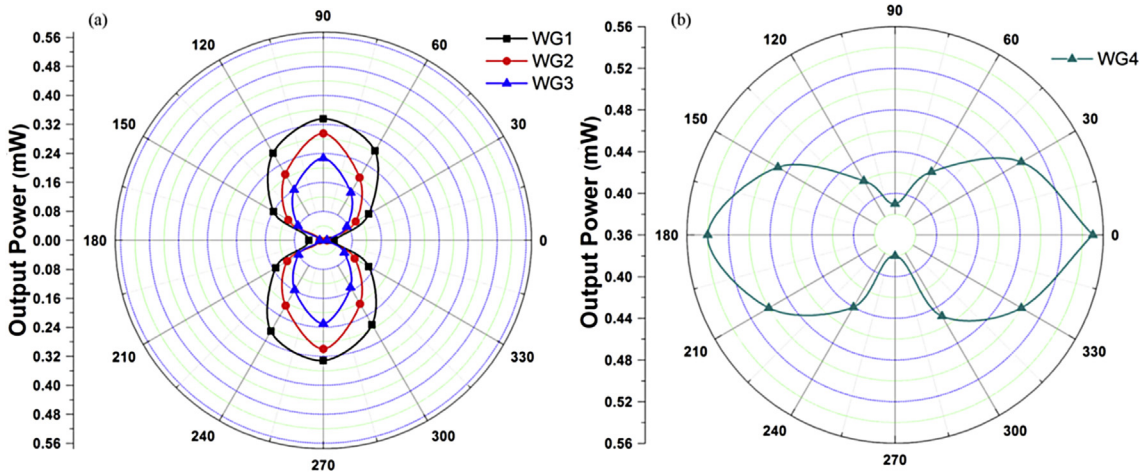

Fig. 4. The Polar images of the output light power of (a) the dual-line waveguides WG1-WG3 and (b) the cladding waveguide WG4 and the corresponding fits (lines) at 632.8 nm with the input light power of 1.585 mW.

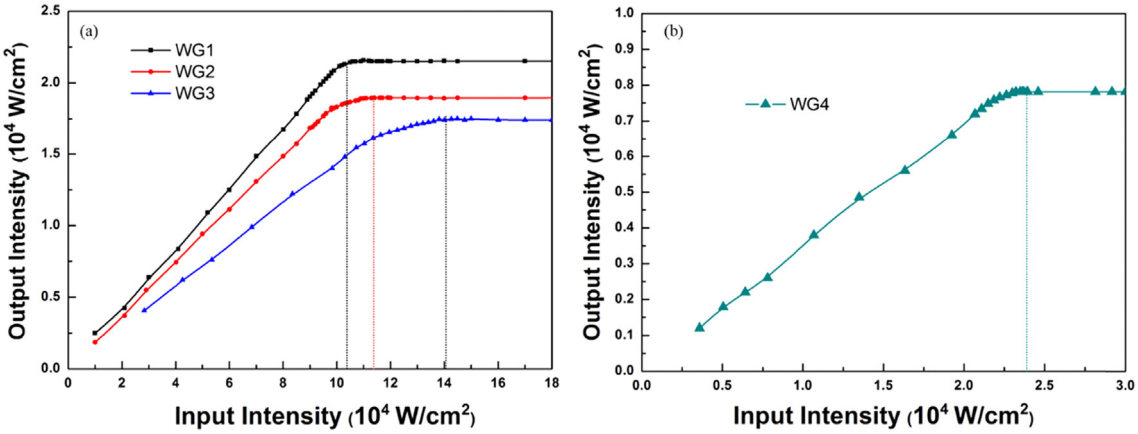

Fig. 5. Intensities of output light as function of those of the input light of the (a) the dual-line waveguides WG1-WG3 and (b) the cladding waveguide WG4 of MgO:$LiNbO_3$.

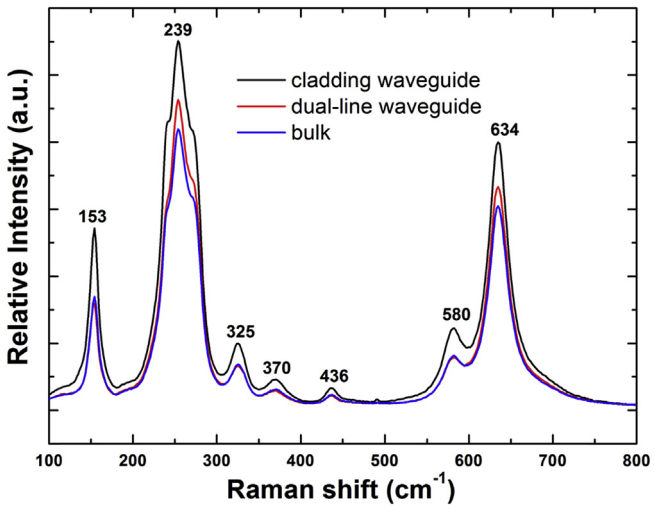

Fig. 6. Confocal micro-Raman spectra obtained from the dual-line waveguide region (WG1, red solid line), cladding waveguide region (WG4, black solid line) and bulk region (blue solid line) in the MgO:$LiNbO_3$ crystal. (For interpretation of the references to colour in this figure legend, the reader is referred to the web version of this article.)

femtosecond laser micromachining exhibit higher optical-damage resistance, which indicates that the laser written Mg^{2+}-doped $LiNbO_3$ waveguides will be excellent candidates for chip-scale nonlinear applications.

Acknowledgements

The work was supported by the National Natural Science Foundation of China (Nos.11274203, and 11511130017) and Spanish Ministerio de Educacion y Ciencia (FIS2013-44174-P).

References

[1] R.V. Schmidt, I.R. Kaminow, Appl. Phys. Lett. 25 (1974) 458–460.
[2] C. Canali, A. Carnera, G.D. DellaMea, P. Mazzoldi, S.M. Al Shukri, A.C.G. Nutt, R.M. De La Rue, J. Appl. Phys. 59 (1986) 2643–2649.
[3] F. Wehrmann, C. Harizi, H. Herrmann, U. Rust, W. Sohler, S. Westenho, IEEE J. Sel. Top. Quant. 2 (1996) 263–269.
[4] I. Nee, O. Beyer, M. Müller, K. Buse, J. Opt. Soc. Am. B 20 (2003) 1593–1602.
[5] W.K. Kim, W.S. Yang, H.Y. Lee, Opt. Express 12 (2004) 2568–2573.
[6] E.J. Murphy, Integrated Optical Circuits and Components: Design and Applications, Marcel Dekker, New York, 1999.
[7] G. Zhong, J. Jin, Z. Wu, in: Proceedings of the 11th International Quantum Electronics Conference, IEEE, New York, 1980, pp. 631–632.
[8] D.A. Bryan, R. Gerson, H.E. Tomaschke, Appl. Phys. Lett. 44 (1984) 847–849.
[9] D. Jaque, E. Cantelar, G. Lifante, Appl. Phys. B 88 (2007) 201–204.
[10] Y. Tan, Q. Luan, F. Liu, S. Akhmadaliev, S. Zhou, F. Chen, Opt. Express 21 (2013) 13992–13997.
[11] F. Chen, Laser Phot. Rev. 6 (2012) 622–639.
[12] P.D. Townsend, P.J. Chandler, L. Zhang, Optical Effects of Ion Implantation, Cambridge University Press, Cambridge, 1994.
[13] R.R. Gattass, E. Mazur, Nat. Photonics 2 (2008) 219–225.
[14] K.M. Davis, K. Miura, N. Sugimoto, K. Hirao, Opt. Lett. 21 (1996) 1729–1731.
[15] M. Ams, G.D. Marshall, P. Dekker, J.A. Piper, M.J. Withford, Laser Phot. Rev. 3 (2009) 535–544.
[16] D. Choudhury, J.R. Macdonald, A.K. Kar, Laser Photonics Rev. 8 (2014) 827–846.
[17] T. Calmano, S. Müller, IEEE J. Sel. Top. Quantum Electron. 21 (2015) 1602213.
[18] R. Osellame, G. Cerullo, R. Ramponi, Femtosecond-laser Micromachining: Photonic and Microfluidic Devices in Transparent Materials, Springer, Berlin, 2012.
[19] D.M. Krol, J. Non Cryst. Solids 354 (2008) 416–424.
[20] A. Ferrer, V. Diez-Blanco, A. Ruiz, J. Siegel, J. Solis, Appl. Surf. Sci. 254 (2007) 1121–1125.
[21] A.H. Nejadmalayeri, P.R. Herman, J. Burghoff, M. Will, S. Nolte, A. Tünnermann, Opt. Lett. 30 (2005) 964–966.
[22] S.M. Eaton, H. Zhang, M.L. Ng, J. Li, W.J. Chen, S. Ho, P.R. Herman, Opt. Express 16 (2008) 9443–9458.
[23] J. Siebenmorgen, K. Petermann, G. Huber, K. Rademaker, S. Nolte, A. Tünnermann, Appl. Phys. B 97 (2009) 251–255.
[24] M. Ams, G.D. Marshall, M.J. Withford, Opt. Express 14 (2006) 13158–13163.
[25] M. Will, S. Nolte, B.N. Chichkov, A. Tünnermann, Appl. Opt. 41 (2002) 4360–4364.
[26] F. Chen, J.R. Vazquez de Aldana, Laser Photonics Rev. 8 (2014) 251–275.
[27] L. Gui, B. Xu, T.C. Chong, IEEE Phot. Technol. Lett. 16 (2004) 1337–1339.
[28] J. Burghoff, C. Grebing, S. Nolte, A. Tünnermann, Appl. Surf. Sci. 253 (2007) 7899–7902.
[29] A. Ródenas, L.M. Maestro, M.O. Ramìrez, G.A. Torchia, L. Roso, F. Chen, D. Jaque, J. Appl. Phys. 106 (2009) 013110–013116.
[30] A.R. Mickelson, Guided Wave Optics, Van Nostrand Reinhold, New York, 1993.
[31] J. Siebenmorgen, K. Petermann, G. Huber, K. Rademaker, S. Nolte, A. Tünnermann, Appl. Phys. B 97 (2009) 251–255.
[32] Q. An, Y. Ren, Y. Jia, J.R. Vázquez de Aldana, F. Chen, Opt. Mater. Express 3 (2013) 466–471.
[33] Rsoft Design Group, Computer Software BeamPROP version 8.0, http://www.rsoftdesign.com.
[34] D. Yevick, W. Bardyszewiski, Opt. Lett. 17 (1992) 329–330.
[35] R. He, Q. An, Y. Jia, G.R. Castillo-Vega, J.R. Vzquez de Aldana, F. Chen, Opt. Mater. Express 3 (2013) 1378–1384.
[36] C. Zhang, J. Yang, F. Chen, Y.F. Kong, Nucl. Instrum. Methods Phys. Res. B 286 (2012) 209–212.